

## Mid-Infrared Outbursts in Nearby Galaxies: Nuclear Obscuration and Connections to Hidden Tidal Disruption Events and Changing-Look Active Galactic Nuclei

SIERRA A. DODD,<sup>1</sup> ARYA NUKALA,<sup>2,1</sup> ISABEL CONNOR,<sup>1</sup> KATIE AUCHETTL,<sup>3,4,1</sup> K.D. FRENCH,<sup>5</sup> JAMIE A.P. LAW-SMITH,<sup>6,7</sup> ERICA HAMMERSTEIN,<sup>8,9,10</sup> AND ENRICO RAMIREZ-RUIZ<sup>1</sup>

<sup>1</sup>*Department of Astronomy and Astrophysics, University of California, Santa Cruz, CA, 95064, USA*

<sup>2</sup>*Castilleja School, Palo Alto, CA, 94301, USA*

<sup>3</sup>*School of Physics, The University of Melbourne, Parkville, VIC 3010, Australia*

<sup>4</sup>*ARC Centre of Excellence for All Sky Astrophysics in 3 Dimensions (ASTRO 3D)*

<sup>5</sup>*Department of Astronomy, University of Illinois, 1002 W. Green St., Urbana, IL, 61801, USA*

<sup>6</sup>*Department of Astronomy and Astrophysics, University of Chicago, Chicago, IL, 60637, USA*

<sup>7</sup>*Kavli Institute for Cosmological Physics, University of Chicago, Chicago, IL, 60637, USA*

<sup>8</sup>*Department of Astronomy, University of Maryland, College Park, MD 20742, USA*

<sup>9</sup>*Astrophysics Science Division, NASA Goddard Space Flight Center, 8800 Greenbelt Road, Greenbelt, MD 20771, USA*

<sup>10</sup>*Center for Research and Exploration in Space Science and Technology, NASA/GSFC, Greenbelt, MD 20771, USA*

### ABSTRACT

We study the properties of galaxies hosting mid-infrared outbursts in the context of a catalog of five hundred thousand galaxies from the Sloan Digital Sky Survey. We find that nuclear obscuration, as inferred by the surrounding dust mass, does not correlate with host galaxy type, stellar properties (e.g. total mass and mean age), or with the extinction of the host galaxy as estimated by the Balmer decrement. This implies that nuclear obscuration may not be able to explain any over-representation of tidal disruption events in particular host galaxies. We identify a region in the galaxy catalog parameter space that contains all unobscured tidal disruption events but only harbors  $\lesssim 11\%$  of the mid-infrared outburst hosts. We find that mid-infrared outburst hosts appear more centrally concentrated and have higher galaxy Sérsic indices than galaxies hosting active galactic nuclei (AGN) selected using the BPT classification. We thus conclude that the majority of mid-infrared outbursts are not hidden tidal disruption events but are instead consistent with being obscured AGN that are highly variable, such as changing-look AGN.

*Keywords:* black hole physics — galaxies: active — galaxies: evolution — galaxies: nuclei

### 1. INTRODUCTION

The luminosity of supermassive black holes residing in the nucleus of most if not all galaxies is directly related to the rate at which they are supplied with matter. The fraction of supermassive black holes (SMBHs) that are in a highly luminous state has been observed to peak a few billion years after the Big Bang (Fan et al. 2001; Merloni et al. 2014) and to gradually decline to the present day, where only one black hole out of every one hundred radiates close to its maximum allowed luminosity (Ho 2008). However, most SMBHs in the local universe still show some degree of activity (Heckman & Best 2014), ranging from outbursts with modest luminosities to highly luminous flares.

Black hole activity in the local universe has previously been associated with gas-rich mergers (Canalizo & Stockton 2001), which is thought to power SMBH

growth in the early universe. However, AGN activity has been shown not to correlate with merger activity (demonstrated for type II Seyfert hosts in Kauffmann et al. 2003), and many SMBHs live in gas-poor environments that may be incapable of powering highly variable outbursts (Ho 2008; Kormendy & Ho 2013). This is one of the main reasons why tidal disruption events (where a star approaches a SMBH close enough to be torn apart by tidal forces) are commonly invoked to explain some highly variable SMBH activity in the local universe (Milosavljević et al. 2006; Auchettl et al. 2018). It has been recently argued that SMBHs in the local universe accrete depending on how recent their last episode of star formation occurred (Kauffmann et al. 2003), which also seems to have profound consequences for moderating the rate of tidal disruption events (French et al. 2017; Law-Smith et al. 2017; French et al. 2020; Dodd et al. 2021).

At high redshift, black hole activity is primarily driven by the accretion of gas, which is plentiful in the early universe as compared to today (Ferrarese & Ford 2005). Thus, there clearly exists a transition in how black holes are fed when the gas content of galaxies is drastically reduced (Bongiorno et al. 2012; Mullaney et al. 2012). Yet, the material surrounding accreting supermassive black holes is thought to be related to the active galactic nucleus with its host galaxy (Trump et al. 2015). For this reason, to probe the AGN–host galaxy connection directly in the local Universe, one needs to understand the structure and kinematics of the parsec-scale dust and gas that surrounds accreting SMBHs (Kormendy & Ho 2013).

During the last decade, mid-infrared interferometry has represented a major step forward in the characterization of nuclear dust in nearby AGNs (Ramos Almeida & Ricci 2017). Our current understanding of the close environment of accreting supermassive black holes obtained from infrared and X-ray studies of local active galactic nuclei suggests that the structure of the surrounding gas is complex, clumpy, and highly variable (Ramos Almeida & Ricci 2017; Hickox & Alexander 2018; Toba et al. 2021).

Although scarcely explored, mid-infrared outbursts hold the potential of revealing some of the most dramatic obscured AGN activity, such as the disruptions of stars by SMBHs. What is more, they can be used to directly probe the parsec-scale dust and gas content in nearby AGN and explore the AGN–host galaxy connection for highly variable accretion episodes in nearby galaxies. In this *Letter*, we study the properties of galaxies hosting mid-infrared outbursts in the local Universe, presented in §2.2, in the context of a catalog of five hundred thousand galaxies from the Sloan Digital Sky Survey, described in §2.1, with the goal of constraining their origin.

## 2. METHODS

### 2.1. Reference Catalog

We use the galaxy catalog from Law-Smith et al. (2017) and Dodd et al. (2021). It consists of  $\approx 5 \times 10^5$  galaxies from the Sloan Digital Sky Survey Data Release 7 MPA-JHU catalog<sup>1</sup> (Brinchmann et al. 2004) with additional derived properties from Simard et al. (2011) and Mendel et al. (2014), yielding a wide range of host galaxy properties. These include velocity dispersion, emission line fluxes, Lick  $H\delta_A$ , and star formation rate (SFR) from the MPA-JHU catalog; redshift, bulge

$g - r$ , bulge and galaxy magnitudes, galaxy half-light radius, galaxy Sérsic index, bulge to total light fraction, galaxy asymmetry indicator and galaxy inclination from Simard et al. (2011); and bulge and total stellar masses from Mendel et al. (2014). Line fluxes in the catalog are calculated using the methodology described in Section 2.1 of Tremonti et al. (2004) and are corrected for stellar absorption features. We derive SMBH masses using the  $M_{\text{bh}}-\sigma_e$  scaling relation from Kormendy & Ho (2013). We refer the reader to Law-Smith et al. (2017) for additional discussion.

A sample of AGN is selected from the host galaxy catalog using the BPT classification (Kauffmann et al. 2003; Kewley et al. 2006), which considers the relative strength of OIII (5007Å), H $\beta$ , NII (6584Å), and H $\alpha$  emission lines to infer AGN activity. We require the signal-to-noise for each of these lines to be  $\geq 3$ , yielding a final sample of  $\approx 5 \times 10^4$  AGN.

### 2.2. MIRONG

Jiang et al. (2021) conducted a systematic search of low-redshift ( $z < 0.35$ ) galaxies that sustained mid-infrared outbursts based on *Wide-field Infrared Survey Explorer* (WISE) light curves, yielding a sample of 137 mid-infrared outbursts in nearby galaxies (MIRONG). 103 of the 137 MIRONG from Jiang et al. (2021) are contained in our reference catalog and constitute our MIRONG sample. They are listed in Table 1. Because the Jiang et al. (2021) MIRONG sample is constructed from galaxies in the SDSS spectroscopic catalog with  $z < 0.35$ , we recover a high fraction of matches with the original sample.

Of our 103 MIRONG sample, 3 were previously reported turn-on changing-look AGN (CL AGN): J0915+4814, J1133+6701, and J1115+0544 (Frederick et al. 2019; Yang et al. 2018; Yan et al. 2019). We also recover 4 unclassified optical transients (J0045-0047, J0841+0526, J1533+2729, J1647+3843) and 1 spectroscopically-confirmed supernova (J1540+0054/ASASSN-16eh).

Wang et al. (2022) obtain multi-epoch follow-up spectra of 54 of the 137 originally reported MIRONG, of which 43 are in our host galaxy sample. They propose tentative classifications of either turn-on CL AGN, AGN flare, or TDE for the 22 MIRONG exhibiting emission line variability, 16 of which are in our sample. Based on their analysis, 9 of the 16 in our sample are tentatively classified as TDEs, 5 as non-specified AGN flares, and 2 as turn-on CL AGN.

Studying the host galaxy properties of MIRONG provides us with an alternative classification scheme to constrain their possible identities, for those with and with-

<sup>1</sup> <http://wwwmpa.mpa-garching.mpg.de/SDSS/DR7>

out spectroscopic follow-up. This can be effectively done if nuclear obscuration is fairly independent of galaxy type. We turn our attention to this critical issue in Section 4. In summary, we set out to analyze the host galaxy properties of 103 MIRONG, 43 of which have additional follow-up spectroscopy as described in Wang et al. (2022), with the goal of further understanding their hidden origin.

### 3. HOST GALAXY PROPERTIES

We begin by considering the star formation rate (SFR) and total stellar mass,  $M_*$ , of the host galaxies of MIRONG in relation to our galaxy catalog (see the top panels of Figure 1). We also include in our comparison a sample of 15 CL AGN from Dodd et al. (2021), as well as a sample of TDEs. This includes 8 TDEs from Law-Smith et al. (2017) and 7 TDEs from the Zwicky Transient Facility (ZTF) that are contained in our reference catalog (AT2018hyz, AT2019azh, AT2020ocn, AT2020wey, AT2020vwl, AT2021nwa, and AT2020neh; see, e.g., Hammerstein et al. (2023); Yao et al. (2023), and references therein). From here on out, we refer to these TDE sub-samples by the first initial and year of publication (i.e. LS17, H23, and Y23). We note that although there are TDEs in common between the works of H23 and Y23, we refer to any shared TDEs by Y23 for consistency with later host galaxy analysis of this sample in Section 5.3.

We define the star-forming main sequence (SFMS) of galaxies in this plane to fall along the solid blue line (Peng et al. 2010). Dashed lines spaced by  $1\sigma$  (the median scatter in the SFR measurements) are added to indicate degrees of quiescence. Contours of galaxies and AGN plotted in Figure 1 and throughout this analysis are spaced by  $0.5\sigma$  (11.8%; note that percentages associated with  $\sigma$  in 2D histograms differ from 1D).

Two distinct groupings of galaxies are observed in the SFR -  $M_*$  plane for galaxies (upper left panel of Figure 1). The first, located in the top left and along the SFMS, consists of spiral, late-type galaxies. The SFMS provides a critical tool for studying the quenching of star formation (e.g., Brinchmann et al. 2004) and the possible emergence of quiescent galaxies (as indicated by the second grouping in the lower right). Although the exact process by which this transformation takes place is debated, galaxies falling between late- and early-type galaxies are understood to be in a state of transition (Martin et al. 2007), and are often referred to as *green valley* galaxies. Following Law-Smith et al. (2017) and Dodd et al. (2021), we designate the green valley region as falling between the lower blue dashed line and the orange dashed line in the SFR -  $M_*$  plane.

Before we consider how the various populations relate to one another in this plane, it is important to consider any selection biases that could prevent fair comparison. MIRONG are selected with SDSS as the parent sample, which makes them consistent with our main catalog and AGN subset (see Figure 6 and Appendix A for a comparison of host stellar masses and redshift distributions of these samples). The selection methodology for TDEs in transient surveys, however, biases them toward fainter host galaxies than a typical galaxy in our catalog. For that reason, although we include the TDEs for context and consistency with previous works, we caution against directly comparing TDEs to MIRONG in this plane. We investigate the relationship between MIRONG and TDEs by constructing an unbiased galaxy catalog in Section 5.3.

AGN are generally seen to activate preferentially in SF galaxies (Ho 2008; Kormendy & Ho 2013), and persist through (and possibly drive) the eventual quenching phase (see the upper right panel of Figure 1). As expected, the distribution of MIRONG appears to be more closely aligned in the SFR -  $M_*$  plane with AGN than galaxies. The MIRONG hosts also do not exhibit any large degrees of clumping or grouping like that seen in CL AGN hosts (although the larger sample size is certainly relevant), but the populations do appear to slightly overlap.

As clearly seen in Figure 1, TDEs are observed to preferentially take place in post-starburst host galaxies, also known as E+A galaxies (French et al. 2016; Law-Smith et al. 2017). These unique hosts can be identified through the  $H\alpha$  equivalent width vs. Lick  $H\delta_A$  absorption plane.  $H\alpha$  equivalent widths are associated with current star formation, while Lick  $H\delta_A$  absorption results primarily from A-type stars. E+A galaxies lie in the bottom right of this plane, as seen in the lower panels of Figure 1, where low values of  $H\alpha$  equivalent width indicate little to no ongoing star formation, and high values of Lick  $H\delta_A$  absorption indicate a starburst in the last  $\approx 1$  Gyr. As in French et al. (2016) and Law-Smith et al. (2017), we define E+A galaxies as residing in the rectangle created by the solid black lines in the lower panels of Figure 1 and Balmer-strong quiescent galaxies as those falling in the larger rectangle created by the dashed black lines.

Law-Smith et al. (2017) demonstrated that the over-representation of TDEs in post-starburst galaxies persists even after controlling for black hole mass, redshift, presence of a strong AGN, bulge colors, and surface brightness of host galaxies. French et al. (2016) and Graur et al. (2018) also found rate enhancements of TDEs in quiescent Balmer-strong galaxies, the rates

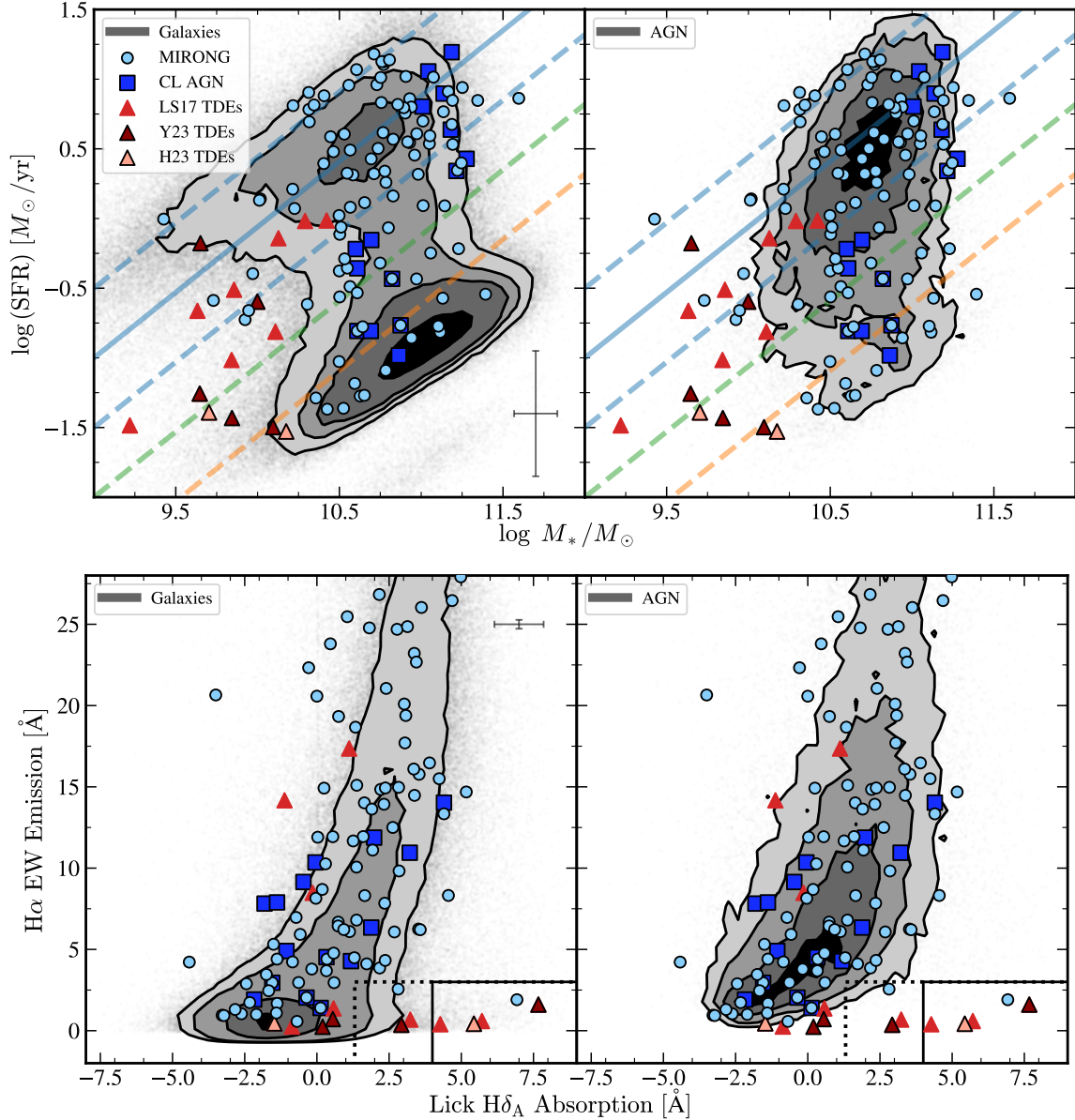


**Figure 1. Top panels:** Star formation rate (SFR) vs. total stellar mass ( $M_*$ ) with galaxies (left) and AGN (right) as contours, with MIRONG (light blue circles), CL AGN (dark blue squares), and TDEs (all triangles; Law-Smith et al. (2017) in red, Hammerstein et al. (2023) in pink, and Yao et al. (2023) in maroon). Following Law-Smith et al. (2017) and Dodd et al. (2021), the star-forming main sequence region is defined according to Peng et al. (2010) and designated by the solid blue line. Each line shown is separated by  $1\sigma$  in SFR. Descending in SFR, the green valley is denoted as the region between the lower blue dashed line and above the dashed orange line. The median error in SFR and  $M_*$  is shown in the bottom right of the left plot. MIRONG appear to closely follow the general AGN population, with a particular grouping in the highly-star-forming region. 3 of the 4 listed turn-on MIRONG are contained in our CL AGN sample: J1115+0544, J0915+4814, and J1133+6701. **Bottom panels:**  $H\alpha$  equivalent width (EW) versus Lick  $H\delta_A$  absorption for the same populations. The rectangle created by the solid lines demarcates E+A galaxies, while the larger rectangle created by the dotted region more broadly designates quiescent Balmer-strong galaxies (French et al. 2016; Law-Smith et al. 2017). Median error is shown in the top right of the left plot. For consistency with Law-Smith et al. (2017), the maximum  $H\alpha$  EW is capped at 28 angstroms. However, 13 MIRONG have  $H\alpha$  EW emission values exceeding this limit and thus are not shown. Such elevated values indicate that a subgroup of MIRONG is more highly-SF than typical AGN. Interestingly, 1 TDE from Yao et al. (2023) (AT2020neh) also has a  $H\alpha$  EW value in excess 28 angstroms. We caution that a direct comparison between the contours shown and the galaxies hosting various transient populations can only be made when the underlying selection mechanisms are taken into account. This is particularly relevant for TDE hosts (Section 5.3) but less important for CL AGN and MIRONG hosts (Section A).

of which were demonstrated by French et al. (2020) to all be consistent with one another, although Hammerstein et al. (2021) found that additionally controlling for green valley preference can account for this over-representation in ZTF-I TDE hosts. Again, although we caution against drawing direct comparisons between the two samples given the TDE host preference for fainter galaxies (the reader is referred to Section 5.3), MIRONG generally do not appear to share TDE hosts' over-representation in the quiescent Balmer-strong region. As in the SFR -  $M_*$  plane, MIRONG hosts seem to broadly follow the distribution of AGN.

Whether the over-representation of TDEs in post-starburst galaxies is physically driven or the result of observational biases is the subject of ongoing study. Tadhunter et al. (2017) suggest that the intrinsic rate of TDEs in highly SF galaxies can dominate over that in post-starburst galaxies, but that high nuclear dust content in such galaxies could make detection extremely difficult. Roth et al. (2021) also find that surveys such as ZTF may account for only  $\sim 30\%$  of TDEs that would be detectable if no dust were present in their host galaxies. Are TDEs in SF galaxies preferentially obscured? It is to this question that we next turn our attention to by studying nuclear obscuration as a function of galaxy type and interstellar extinction.

#### 4. NUCLEAR OBSCURATION, GALAXY TYPE AND GALACTIC-SCALE EXTINCTION

The derived dust properties in the nuclear region of MIRONG hosts (Jiang et al. 2021) allow us to investigate the possibility that TDEs in high dust-content galaxies might be preferentially hidden. Dust mass is derived by assuming that thermal emission from dust is powering the MIR emission. The assumed dust grain size distribution comes from Mathis, Rumpl, and Nord (MRN; Mathis et al. 1977) and is roughly power-law in nature. W1 and W2 fluxes are then fit to a modified blackbody to obtain dust temperature and corresponding masses under the assumption of a high dust covering fraction (Jiang et al. 2021). This assumption seems to be additionally supported by our findings that dust mass is not correlated with galaxy orientation in our galaxy host sample. Because the methodology for deriving dust mass estimates is applied uniformly to all MIRONG, additional factors such as possible differences in individual galaxy dust composition are not taken into account. As such we focus our following analysis on dust mass properties of MIRONG on a population rather than individual level.

To investigate how nuclear dust mass varies with galaxy type, we revisit the SFR -  $M_*$  plane, now with

each MIRONG shaded according to their dust mass content (in units of  $\log M_\odot$ ; see the upper panels of Figure 2). Contours of AGN are shown in the background. No obvious trend is visible between the location on the evolutionary sequence of galaxies and nuclear dust mass. As discussed in the previous section, it has been suggested that TDEs could occur at elevated rates in highly SF galaxies but would be obscured by higher levels of nuclear dust (Tadhunter et al. 2017). Since TDEs are preferentially observed in green valley host galaxies, we compare the nuclear dust content of SFMS and green valley MIRONG galaxies in the upper right panel of Figure 2 to see whether nuclear dust levels are elevated in highly SF galaxies. The two distributions are similar, as also seen by their median values (solid black lines) and  $\pm 1\sigma$  (dashed black lines). We perform a Kolmogorov-Smirnov test on the two samples. The resultant p-value of 0.37 implies that we are unable to reject the null hypothesis that the two populations are drawn from the same underlying distribution, suggesting they are consistent with one another. This is in stark contrast to predictions that advocate for an elevated rate of obscured TDEs in SF galaxies. We also find no trend between  $D_n(4000)$ , an indicator of the age of the galaxy stellar population (Kauffmann et al. 2003), and nuclear dust mass. We can thus conclude that nuclear obscuration does not correlate with stellar properties such as stellar mass and age. Combined with the finding that nuclear dust does not depend on SFR, we can conclude that obscured TDEs would not prefer one type of galaxy over another. This implies we are not missing a population of TDEs in more highly-SF galaxies, and that their observed green valley preference might be based on underlying physical mechanisms controlling the rate of TDEs (see, e.g., Law-Smith et al. 2017, and references therein).

Having shown that nuclear obscuration does not depend on galaxy type, here we consider how the Balmer decrement, which is thought to correlate with the dust mass content in a galaxy, correlates with the abundance of dust surrounding SMBHs. Balmer decrement, which consists of the ratio between  $H\alpha$  and  $H\beta$  emission lines from the Balmer series ( $n=2$ ), is commonly used as a measure of galaxy interstellar extinction. However, the presence of an AGN can alter the region probed by this measurement. To this end, the Balmer decrement has been used to measure dust extinction in the broad line regions of type I AGN and quasars (Dong et al. 2008; Ma et al. 2023), as well as in the narrow line region of AGN (Lu et al. 2019). For partially obscured AGN, such as the ones in our MIRONG sample, we can expect the Balmer decrement to reflect extinction on both nuclear and galactic scales. Because most of the MIRONG in

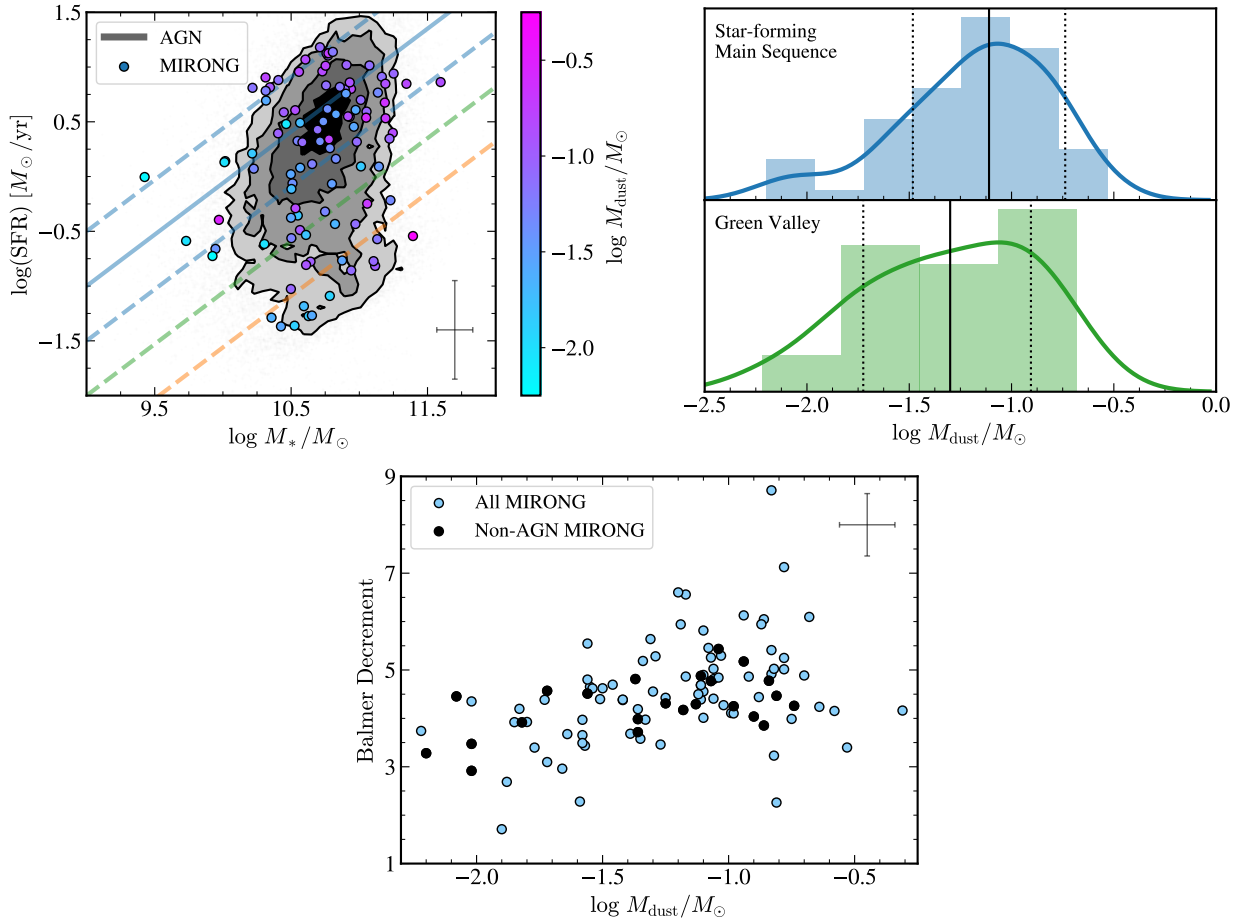


**Figure 2.** **Top left:** Star formation rate vs. total stellar mass as seen in the top panel of Figure 1, this time with only AGN contours and MIRONG scatter points. The colorbar indicates derived log dust mass from Jiang et al. (2021) in units of  $M_{\odot}$ . **Top right:** Histogram of log dust mass for MIRONG lying in the SFMS (top) and green valley (bottom). Solid lines represent the median of each distribution, and dotted lines are spaced  $\pm 1\sigma$  from the median. The two distributions are broadly consistent with one another, indicating that nuclear dust of MIRONG host galaxies does not vary with galaxy type. One outlying MIRONG (J154029.29+005437.2) has been excluded from all plots in this figure and is found in the green valley with a log dust mass of -3.71. Including this MIRONG only serves to broaden the standard deviations and leaves the median in place. **Bottom:** Balmer decrement vs. log dust mass for MIRONG host galaxies. The error bar in the top right represents the median error value for all MIRONG host galaxies in each parameter. Errors for Balmer decrement measurements are calculated from the error in  $H\alpha$  and  $H\beta$  line flux measurements multiplied by the recommended MPA-JHU uncertainty scaling factors of 2.473 (for  $H\alpha$ ) and 1.882 (for  $H\beta$ ).

our sample (76; 52 of which have strong ( $\geq 3$ ) signal-to-noise ratio in the BPT line measurements) are classified as AGN in the BPT diagram, we expect a large degree of scatter in their Balmer decrements.

The bottom panel of Figure 2 shows the Balmer decrement of all MIRONG vs. nuclear log dust mass, separated into galaxy hosts with and without AGN activity. As anticipated, we see a large degree of scatter in the AGN group. The non-AGN show considerably less scatter. Neither group shows a strong correlation be-

tween Balmer decrement and nuclear dust mass<sup>2</sup>. As the Balmer decrements of the non-AGN group are more likely to be indicative of galactic-scale dust, this suggests no clear correlation between nuclear- and galactic-scale dust in these systems. This is in agreement with works such as Merloni et al. (2014), which find that the de-

<sup>2</sup> This statement is supported by correlation coefficients  $\lesssim 0.5$  for each population in both Pearson and Spearman tests (Correlation coefficient values: AGN MIRONG Pearson = 0.39, AGN MIRONG Spearman = 0.41, non-AGN MIRONG Pearson = 0.53, non-AGN MIRONG Spearman = 0.37.). We note that the highest correlation coefficient of 0.53 for non-AGN MIRONG could be consistent with a weak correlation with significant scatter.

gree of nuclear obscuration appears uncorrelated with larger-scale galactic properties including SFR and total stellar mass. This provides an additional clue that the dust content of galaxies in the local Universe at the host scale does not determine their innermost dust content.

## 5. ON THE ORIGIN OF MIRONG SOURCES

Finding any correlation between nuclear- and galactic-scale dust content is key to understanding any potential host galaxy preference for the MIRONG population. With this information, we can examine the notion that MIRONG in highly SF regions (where galactic dust is expected to be abundant) could plausibly be obscured TDEs that until now we had no means of uncovering. Having proven that nuclear obscuration does not depend on host galaxy type, it is clear that the hidden population should mirror the unobscured population. This enables us to use host galaxy properties of unobscured nuclear transients to identify possible MIRONG origins. In this Section, we explore possible explanations for the origin of the bulk of the MIRONG population, including the fraction of MIRONG that might be TDEs.

### 5.1. CL AGN Matching in the SFR - $M_*$ Plane

We identify MIRONG hosts located within a range of SFR and total stellar mass of CL AGN hosts using the matching methodology of Law-Smith et al. (2017) and Dodd et al. (2021), but with a 10% tolerance window (corresponding to 0.21 in log SFR and 0.07 in log  $M_*$ ). As is customary, for this matching procedure and others that follow, tolerances are chosen to be consistent with the mean separation of sources in the plane of comparison. Table 2 summarizes our findings. We locate 18 MIRONG with matching properties to CL AGN hosts (including recovering the 3 duplicates), corresponding to 17.5% of MIRONG in our sample.

Of the 18 MIRONG with similar host properties to CL AGN, 10 are classified as AGN in the catalog (19.2%; see Section 2 for details on AGN classification). For comparison, the relative percentages of AGN and galaxies near CL AGN hosts are 18.0% and 14.7%, respectively. This implies that the MIRONG population is about as likely to resemble a CL AGN host as a typical AGN. This is perhaps unexpected, given that MIRONG are selected such that they need to be associated with a highly variable nuclear source. Even though MIRONG do not stand out from AGN in this regard, we consider host galaxy Sérsic index as a means of distinguishing between typical AGN and highly variable (HV) AGN (including CL AGN) in the next section.

Most MIRONG hosts broadly resemble the general AGN population in the SFR and  $M_*$  plane. We confirm

this using a 2D Kolmogorov–Smirnov test and are thus unable to reject the null hypothesis that the two samples were drawn from the same distribution (p value: 0.11). This is however not the case when compared to the galaxy population (p value:  $6 \times 10^{-8}$ ). Despite their apparent similarity to typical AGN, the identification of MIRONG via their extreme outbursts points to a more dramatic type of variability than what is expected for typical AGN in the local Universe. CL AGN represent the extreme end of these highly-variable AGN. A useful phenomenological distinction between AGN and highly variable (HV) AGN is galaxy Sérsic index (Dodd et al. 2021). In the following section we thus analyze MIRONG in this context.

### 5.2. Sérsic Index Comparison

Sérsic index measures the light concentration of the galaxy surface brightness. Higher values correspond to highly centrally concentrated light profiles, such as those often exhibited by elliptical galaxies, while lower values are more consistent with diffuse profiles, such as those seen in spirals. Sérsic index is generally thought to provide a measurement of the density profile of stars and, to a lesser extent, the kinematic state of the star-forming gas in the nuclear region (Raouf et al. 2021). As mentioned previously, highly variable AGN and CL AGN have been shown to have higher Sérsic indices than AGN (Dodd et al. 2021), even when controlling for black hole mass. TDE hosts also exhibit this trend to a slightly lesser degree (Law-Smith et al. 2017).

Figure 3 shows Sérsic index for AGN, MIRONG, and CL and HV AGN. The four HV AGN used in our sample are the same from Dodd et al. (2021) and consist of KUG 1624+351 (Khabibullin & Sazonov 2014), J094608+351222 (Graham et al. 2017), 2MASS J09392289+3709438 (Strotjohann et al. 2016), and Swift J1200.8+0650 (Landi et al. 2007). Intriguingly, the last object listed (Swift J1200.8+0650) is also a MIRONG source, even though it was selected independently. The MIRONG distribution differs markedly from that of AGN. MIRONG Sérsic indices tend to fall between those of AGN and CL and HV AGN. We also performed this analysis with a sample of AGN matched to MIRONG based on SFR, total stellar mass, and redshift, and found no noticeable difference in the resulting distribution compared to typical AGN. We also note that although the distribution of Sérsic indices for AGN is slightly higher for active versus inactive galaxies, this has been shown to become less notable for lower-resolution galaxies (with redshifts larger than  $z > 0.05$ ) and thus likely does not strongly influence our findings here (Gadotti 2008). Comparing the distribution of

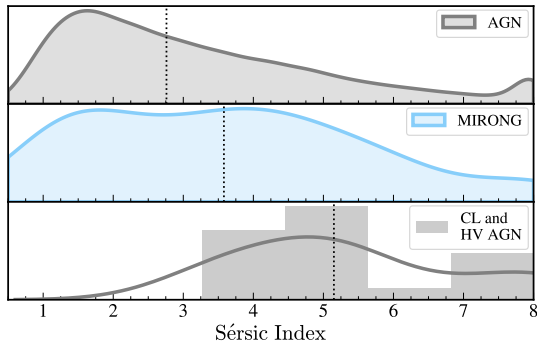


**Figure 3.** Sérsic index smoothed histograms for AGN, MIRONG, and CL + HV AGN host galaxies. The area under the distributions is normalized to 1. Dashed vertical lines represent the median of each distribution. The MIRONG population generally display higher Sérsic indices than typical AGN.

MIRONG Sérsic indices to these other populations suggests that HV AGN are the likeliest source of MIRONG behavior, as opposed to standard AGN-type flares.

### 5.3. The rate of TDEs in the MIRONG population

In order to compare TDE hosts to the MIRONG population, a control galaxy sample must be constructed. We employ the methodology described in Section 2.2 of Hammerstein et al. (2021) to create a sample of SDSS galaxies that can be directly compared to our TDE hosts. We derive the maximum redshifts that SDSS would be complete out to for each of the 33 Y23 TDEs<sup>3</sup>. As in Hammerstein et al. (2021), we cap our SDSS galaxy matches per TDE to be 1000 and resample as needed for TDEs with less than 1000 matches. This constitutes our SDSS TDE reference sample and can be seen in the contours of the left panel of Figure 4, which shows host galaxy color ( $^{0,0}u - r$ ) versus total stellar mass, as in Figure 18 of Yao et al. (2023).  $^{0,0}u - r$  is defined as the difference between the rest frame, galactic extinction-corrected  $u$  and  $r$  absolute magnitudes from the Photoz table in SDSS DR7. The  $^{0,0}u - r$  vs total stellar mass plane also allows for the identification of the green valley region, as described earlier in Section 3, and also allows us to use the full sample of 33 Y23 (as opposed to only using the 5 contained within our original catalog that have SFR measurements). Here the green valley is defined according to Equation 22 from Yao et al. (2023). TDEs are over-represented in the green val-

<sup>3</sup> We note that we perform our analysis using  $g$ - instead of  $r$ -band values as done in Hammerstein et al. (2021). Properties of the resulting galaxy sample are consistent regardless of band choice.

ley of this plane (Yao et al. 2023) as well as in the SFR versus stellar mass plane of Figure 1.

In order to robustly compare the host properties of TDEs in relation to the other populations, we perform the following steps. First, we select TDEs that fall at or within the outer contour of host galaxy color and total stellar mass shown in Figure 4. The outer contour contains 86.4% of the SDSS TDE reference sample. Second, we select MIRONG, CL AGN, and AGN that fall within the same boundary. This ensures that the magnitude limit corrections described above are applied to each of these distinct samples. This yields 37/103 MIRONG (35.5%), 21/33 TDEs (63.6%), 8/15 CL AGN (53.3%), and 29,375/52,613 AGN (55.8%). We now perform the tolerance matching described in the previous section but for TDEs and MIRONG. We use a 9% tolerance range (corresponding to 0.08 in  $^{0,0}u - r$  and 0.10 in  $\log M_*$ ). A sample box size can be seen in the lower right of the left panel of Figure 4. We find 4 matches out of the 37 MIRONG in this SDSS TDE comparison sample (10.8%). A comparison of total stellar masses of the SDSS TDE reference samples can be seen in Figure 7 and is explored in Appendix B.

We can also consider the distribution of the SDSS TDE reference sample-limited AGN, CL AGN, and MIRONG in the host galaxy color versus total stellar mass plane. As seen on the right panel of Figure 4, MIRONG again mirror the general AGN population and occupy a similar region to CL AGN. We note that even in this more restrictive sample that is limited in redshift to account for TDE selection biases, we still find that MIRONG hosts appear much more closely related to AGN than TDEs.

We now examine if our derived rate of TDEs in MIRONG based on host galaxy matching of  $\lesssim 11\%$  is consistent with the classification of MIRONG from Wang et al. (2022). The authors spectroscopically monitored 53 of the 103 original MIRONG sources over a roughly 4-year period. Of these 53, 22 (41.5%) displayed variability in the broad H $\alpha$  emission line (EL). Wang et al. (2022) perform their subsequent classification on this subsample of 22 objects, based on the notion that any light from a transient event located at or near the central, obscured SMBH would have been reprocessed by the dust over this monitoring timescale.

TDEs are selected from this group of 22 EL-variable sources as follows. Sources are split into likely AGN and quiescent groups. Quiescent sources are classified as TDEs with the exception of one turn-on AGN candidate. Any AGN MIRONG with iron coronal lines and He II $\lambda$ 4686 features are also tentatively classified as TDEs given the association of those features with



TDE spectra (Leloudas et al. 2019). This results in 14 TDE candidates ( $\approx 26\%$ ).

The authors highlight the challenges associated with classifying obscured nuclear transients. This includes the possibility of a myriad of origins for AGN flares, for which we have very few expected spectral templates for comparison (although much progress has been made recently, see, e.g., Clark et al. (2023)). As such, we hope to offer a complementary view to the work of Wang et al. (2022) based on host galaxy properties of unobscured TDEs. We have 6 of the 14 Wang et al. (2022) TDE candidates in our entire galaxy catalog, but none within the SDSS TDE reference sample. Although we are unable to directly compare the TDE candidates from Wang et al. (2022) to our SDSS TDE reference sample, the overall relatively low fraction of MIRONG with similar host properties to unobscured TDEs ( $\approx 11\%$ ) suggests that, as the authors posit, there is likely other variability at play that can drive MIRONG flares besides TDEs, including HV AGN-type flares.

Finally, an additional estimate of the rate of TDEs in MIRONG can be made by again utilizing our finding from Section 4 that the obscured hosts should mirror the unobscured population of TDE hosts. Briefly revisiting the bottom panel of Figure 1 and considering the subset of 5 Y23 TDEs that have matches in our host galaxy catalog, we see that very few of the MIRONG occupy the post-starburst region favored by TDEs and shown by the dotted black lines. Using a simple analysis, if 2 out of 5 TDE hosts (40%) lie in this region, and 2 out of 103 MIRONG (1.9%) occupy this region as well, we can estimate the number of obscured TDEs responsible for MIRONG behavior to be somewhere around 5 (4.9%).

## 6. SUMMARY AND CONCLUSIONS

The arguments leading to the conclusion that the bulk of MIRONG are obscured HV AGN can be broadly summarized as follows:

- MIRONG host galaxies appear more similar to AGN host galaxies in the SFR -  $M_*$  plane than galaxies or TDE hosts (Figure 1).
- Nuclear dust content does not appear to correlate with host galaxy type, stellar properties, or galaxy orientation. We also find no strong correlation between nuclear dust content with galactic-scale dust content as estimated by the Balmer decrement in MIRONG host galaxies showing no AGN activity. This suggests that the obscured host galaxy transient population should trace the unobscured one and that we are not missing a population of TDEs in highly SF galaxies (Figure 2). This also im-

plies that the observed post-starburst preference of TDEs is intrinsic, as opposed to an observational bias, raising many questions about the uniqueness of these systems. What is more, we conclude that the intrinsic rate of TDEs in star-forming galaxies is significantly lower than in post-starburst hosts.

- Based on a comparison with the unobscured population, we estimate the relative fraction of TDEs responsible for MIRONG to be  $\lesssim 11\%$  (Figure 4, see Appendix B for a summary of matching results).
- We conclude that the majority of MIRONG appear to be driven by HV AGN activity, as suggested by the higher Sérsic index distribution when compared to typical AGN (Figure 3).

Having shown that TDEs are likely a smaller fraction of MIRONG than originally anticipated and that HV AGN might represent a higher fraction as shown by host galaxy and Sérsic index analyses, we lastly consider whether or not the observed rates of these transient populations are consistent with one another. Figure 5 shows an adapted version of the luminosity function (LF) from Jiang et al. (2021), with the additional inclusion of a population of soft X-ray AGN from Auchettl et al. (2018). The two lines represent fits to the MIRONG population for different assumed dust covering factors: the red line for a factor of 1, the fainter pink line for a factor of 0.3 (both lines from Jiang et al. 2021). As illustrated in Jiang et al. (2021), MIRONG appear similar in rate to optical and X-ray TDE fractions, especially given the uncertainty in the obscuration factor. However, we do note that other X-ray TDE rate estimates may be found to differ from the ones presented here (see, e.g., Sazonov et al. 2021). Soft X-ray AGN exhibit higher values of  $\Phi$  (i.e. have a higher occurrence rate in the local universe) than MIRONG across luminosity bins. Given that HV AGN are by nature a smaller subset of the local AGN population, the LF of MIRONG would likely be consistent with that of HV AGN. This is consistent with our findings that HV AGN could be responsible for most MIRONG.

### 6.1. Relationship between nuclear obscuration and host galaxy properties

The MIRONG population offers us an exciting opportunity to study the observational appearance of obscured AGN and TDEs, which is not only determined by their intrinsic emission properties but also by the state of the intervening material along the line of sight. We find that nuclear dust obscuration does not correlate with host galaxy type or with the extinction of the

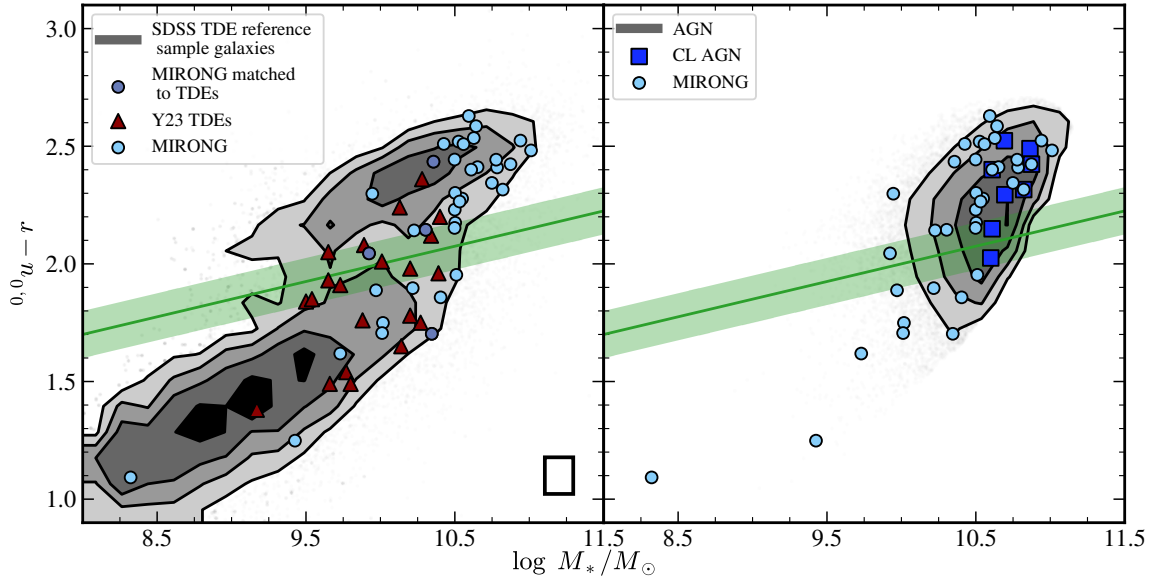


**Figure 4.** Host galaxy color ( $^{0,0}u - r$ ) versus total stellar mass for SDSS TDE reference samples (see Section 5.3 for a detailed explanation of sample selection) with the green valley region in this plane as defined by Yao et al. (2023). **Left:** Galaxy contours with MIRONG, MIRONG near TDE hosts, and TDEs. Matching is performed using the methodology of Law-Smith et al. (2017); Dodd et al. (2021) with a 9% tolerance, yielding 4 MIRONG matches ( $\lesssim 11\%$ ). A box representing the matching size is shown in the lower right. **Right:** AGN contours with MIRONG and CL AGN. We note that even with these additional, restrictive selection criteria, MIRONG generally follow the AGN sample.

host galaxy. This is in agreement with Merloni et al. (2014), which finds no significant difference between the mean stellar masses and star formation rates of obscured and unobscured AGN hosts selected by X-ray flux. In essence, it is commonly understood that the physical state of intervening material is largely insensitive to the wider scale galactic conditions but appears to be mainly determined by radiation properties of the nuclear region (Ricci et al. 2017; GRAVITY Collaboration et al. 2020; Barrows et al. 2021; García-Bernete et al. 2022). For highly luminous AGN, the dust content inferred from the column of material responsible for the X-ray absorption is commonly larger than the one inferred from the reprocessing luminosity. This is consistent with the idea that X-ray absorbing gas is located within the dust sublimation radius, whereas the mid-IR flux arises from an area farther out (Ramos Almeida et al. 2009). Given that the MIRONG population, as argued in this *Letter*, is likely to be associated with highly luminous nuclear activity, we expect the X-ray absorbing region to be located within the dust sublimation radius. Swift J1200.8+0650 provides us with the best example to test this hypothesis, given that it was identified independently by the MIRONG and the high Galactic latitude *Swift* survey. The X-ray absorbing gas measurement in Swift J1200.8+0650 ( $6 - 8 \times 10^{22} \text{ cm}^{-2}$ ; Landi et al. 2007) implies a much higher dust mass than the one derived from the mid-IR luminosity under the assumption

of a high covering factor ( $\approx 0.2M_{\odot}$ ; Jiang et al. 2021). As expected, the dust mass inferences in the MIRONG population are thus likely to be highly sensitive to the physics of dust sublimation. Be that as it may, radiative feedback in Swift J1200.8+0650 and other MIRONG sources is still unable to completely clear out the circumnuclear dust environment. In sources for which the removal of dusty gas might be ultimately efficient, the nuclear source may decline in luminosity, giving rise to unabsorbed sources at lower luminosities.

In closing, here we confirm the general view that there is little physical connection between the gas accreting onto the SMBH and the material out of which stars form throughout the galaxy by demonstrating the lack of a connection between obscuring dust within the sphere of influence of the SMBH and the galaxy-wide properties (stellar age, stellar mass, SFR and dust content). This is consistent, for example, with the findings derived from large comprehensive studies using Herschel (Rosario et al. 2012) and XMM-Newton in the COSMOS field (Merloni et al. 2014).

We thank the referee for incredibly useful comments and suggestions. We would like to express gratitude for insightful discussions with Julianne Dalcanton, Jenny Greene, Ryan Foley, and Morgan MacLeod. S.A.D. and E.R.R. thank the Heising-Simons Foundation, NSF (Graduate Research Fellowship, (AST-

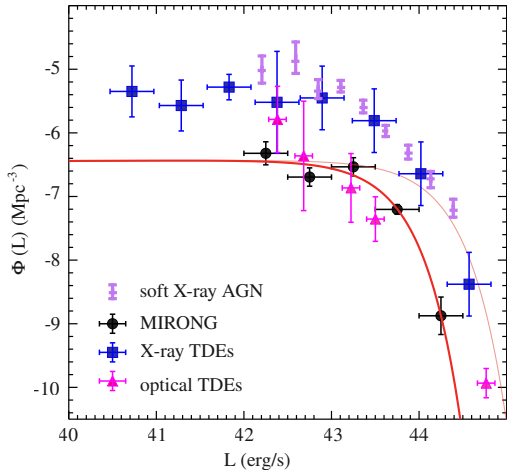


**Figure 5.** Luminosity function for MIRONG for given luminosity bins, adapted from Figure 10 from Jiang et al. (2021). In addition to the X-ray TDEs from Figure 6 of Achetttl et al. (2018) and the optical TDEs from Figure 1 of van Velzen (2018), we additionally include the soft X-ray AGN sample from Achetttl et al. (2018). The red line is a single Schechter function fit to MIRONG, and the fainter pink line represents the expected shift in the MIRONG distribution if a lower dust covering factor of 0.3 is assumed (both from Jiang et al. 2021).

2150255 and AST-2307710)), Swift (80NSSC21K1409, 80NSSC19K1391) and Chandra (22-0142) for support. K.D.F. acknowledges support from NSF grant AST-2206164.

## APPENDIX

### A. HOST GALAXY PROPERTIES OF MIRONG, CL AGN AND AGN IN THE SDSS CATALOG

The host galaxy matching analysis relies on the various methods used to uncover the associated transient population. Since not all transients were uncovered using the same survey or discovery technique, an effective matching sample needs to be constructed. This is the case for our TDE sample, which we present in Section 5.3. As mentioned briefly in Section 3, this is not the case for MIRONG and CL AGN samples, which are primarily selected using the SDSS catalog. Figure 6 gives credence to this idea and highlights the similarities in their distributions of total stellar mass (left) and redshift (right). We find that controlling for either of these properties before performing any matching or comparison described above does not yield differences in our conclusions, as expected given the similarities in their intrinsic distributions.

For completeness, we also refer the reader to Table 1 and Table 2 for a summary of all MIRONG host galaxy properties referenced in this *Letter* as well as for a synopsis of our CL AGN host galaxy matching exercise.

### B. TDE – MIRONG HOST GALAXY MATCHING SUMMARY

We perform two primary matching analyses in this work to constrain the fraction of MIRONG that may be TDEs: one in  $^{0,0}u - r - \log M_*/M_\odot$  (yielding 10.8%) and another in  $H\alpha$  equivalent width (EW) – Lick  $H\delta_A$  absorption (yielding 4.9%). The 10.8% derived from the  $^{0,0}u - r, \log M_*/M_\odot$  matching is the most robust given that it was performed with the largest samples of TDEs and MIRONG (21 and 37, respectively).

Figure 7 shows the distribution of total stellar masses for all SDSS TDE reference samples (see Section 5.3 for more detail). It is clear from this comparison that the TDEs favor lower-mass host galaxies. This continues to be highly prevalent even after we construct the matching sample in order to accurately account for detection biases. Matching MIRONG to TDE hosts in this reference sample yields 37.8% taking only total stellar mass into account. This can be understood as an upper limit to the occurrence of TDEs in MIRONG hosts.

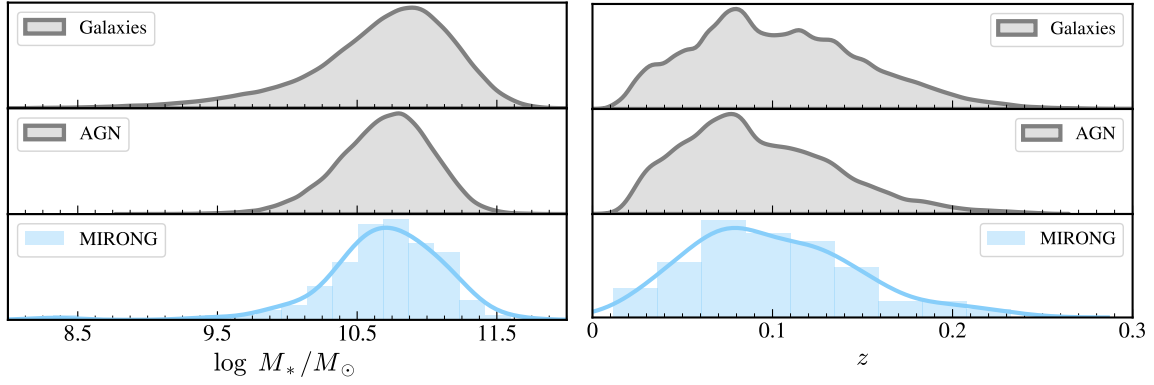


**Figure 6.** Host galaxy comparisons in total stellar mass (left) and redshift (right) for all galaxies, AGN, and MIRONG in our catalog. The similarity between populations in each parameter makes possible the host galaxy comparison analysis that constitutes our methodology.

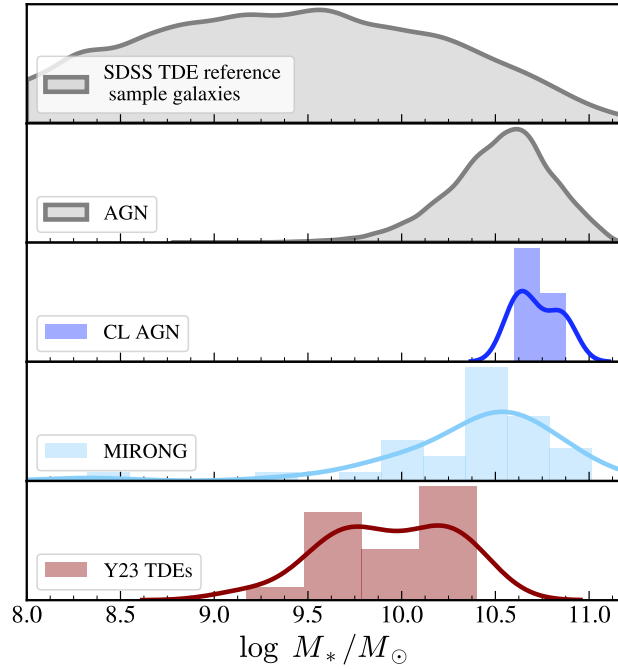


**Figure 7.** Total stellar masses for all SDSS TDE reference samples (see Section 5.3 for a detailed explanation of sample selection), including galaxies, AGN, CL AGN, MIRONG, and Y23 TDEs. Even after controlling for selection effects unique to TDEs compared to the other transients, TDEs favor lower-mass host galaxies.

**Table 1.** MIRONG Sample

SDSS Name	R.A.	Dec	$z$	SFR	$\log M_*/M_\odot$	$\log M_{\text{dust}}$	Sérsic Index	$^{0,0}u-r$
J110501.98+594103.5 <sup>*a</sup>	166.2583	59.6843	0.0337	0.6938	10.316	-1.58	$5.15 \pm 0.04$	1.55
J163246.84+441618.5 <sup>*a</sup>	248.1952	44.2718	0.0579	-1.3619	10.525	-1.88	$4.28 \pm 0.17$	2.52
J165726.81+234528.1 <sup>*a</sup>	254.3617	23.7578	0.0591	-0.3956	9.971	-0.53	$1.74 \pm 0.11$	1.89
J104306.56+271602.1 <sup>*a</sup>	160.7774	27.2673	0.1281	0.1142	10.654	-1.25	$7.96 \pm 0.15$	2.13
J140221.26+392212.3 <sup>*a</sup>	210.5886	39.3701	0.0638	0.3251	10.547	-1.29	$1.23 \pm 0.03$	1.92

Table 1 continued

Table 1 (*continued*)

SDSS Name	R.A.	Dec	$z$	SFR	$\log M_*/M_\odot$	$\log M_{\text{dust}}$	Sérsic Index	$^{0,0}u-r$
J151345.76+311125.0 <sup>*a</sup>	228.4407	31.1903	0.0718	0.5689	10.829	-1.55	$2.50 \pm 0.03$	1.90
J164754.38+384342.0 <sup>*a</sup>	251.9766	38.7283	0.0855	0.2108	10.214	-1.82	$1.85 \pm 0.13$	1.53
J154955.19+332752.0 <sup>*a</sup>	237.4800	33.4644	0.0856	0.1408	10.017	-1.36	$1.27 \pm 0.06$	1.75
J111536.57+054449.7 <sup>*a</sup>	168.9024	5.7471	0.0900	-0.8071	10.610	-0.92	$4.12 \pm 0.22$	2.40
J131509.34+072737.6 <sup>*b</sup>	198.7889	7.4605	0.0918	0.7665	11.136	-1.34	$5.09 \pm 0.10$	1.96
J153711.29+581420.2 <sup>*b</sup>	234.2971	58.2389	0.0936	0.3130	10.583	-1.08	$3.41 \pm 0.19$	2.14
J113355.93+670107.0 <sup>*b</sup>	173.4831	67.0186	0.0397	-0.4329	10.822	-1.66	$3.76 \pm 0.02$	2.32
J133212.62+203637.9 <sup>*b</sup>	203.0526	20.6105	0.1125	1.0122	10.753	-0.78	$5.71 \pm 0.18$	1.79
J123852.87+081512.0 <sup>*b</sup>	189.7203	8.2533	0.1138	0.4280	10.694	-1.11	$3.31 \pm 0.14$	1.86
J100350.97+020227.6 <sup>*c</sup>	150.9624	2.0410	0.1247	-0.0666	10.799	-1.50	$3.91 \pm 0.23$	2.24
J144227.57+555846.3 <sup>*c</sup>	220.6149	55.9795	0.0769	0.8001	10.939	-0.82	$4.11 \pm 0.02$	2.02
J124521.42-014735.4 <sup>*</sup>	191.3393	-1.7932	0.2154	0.5375	11.050	-0.58	$7.81 \pm 0.29$	2.18
110958.34+370809.6 <sup>*</sup>	167.4931	37.1360	0.0260	-1.1838	10.594	-1.72	$4.95 \pm 0.01$	2.63
J155743.52+272753.0 <sup>*</sup>	239.4314	27.4647	0.0316	0.9564	10.558	-0.83	$2.44 \pm 0.01$	2.51
112916.12+513123.5 <sup>*</sup>	172.3172	51.5232	0.0329	0.3398	10.778	-0.78	$1.41 \pm 0.01$	2.44
J160052.26+461242.9 <sup>*</sup>	240.2178	46.2119	0.1974	0.8476	11.191	-0.88	$1.64 \pm 0.15$	2.13
J010320.42+140149.8 <sup>*</sup>	15.8351	14.0305	0.0418	0.5445	10.929	-0.81	$1.01 \pm 0.01$	1.90
J083536.49+493542.7 <sup>*</sup>	128.9020	49.5952	0.0424	-0.3198	10.749	-1.30	$2.73 \pm 0.02$	2.34
J165922.65+204947.4 <sup>*</sup>	254.8444	20.8298	0.0451	0.0911	11.144	-1.46	$2.97 \pm 0.01$	2.30
J120338.31+585911.8 <sup>*</sup>	180.9097	58.9866	0.0469	-0.5879	9.730	-2.02	$1.51 \pm 0.13$	1.62
J130815.57+042909.6 <sup>*</sup>	197.0649	4.4860	0.0483	-1.2743	10.627	-1.85	$4.78 \pm 0.06$	2.53
J105801.52+544437.0 <sup>*</sup>	164.5064	54.7436	0.1306	0.6060	10.530	-0.86	$2.53 \pm 0.24$	1.57
J113901.27+613408.5 <sup>*</sup>	174.7553	61.5691	0.1346	1.0686	10.605	-0.84	$0.95 \pm 0.04$	1.48
J162810.03+481047.7 <sup>*</sup>	247.0419	48.1799	0.1245	0.7825	10.314	-1.25	$1.17 \pm 0.06$	1.56
J132259.94+330121.9 <sup>*</sup>	200.7498	33.0227	0.1269	0.7953	10.893	-1.10	$1.03 \pm 0.05$	2.14
J112018.31+193345.8 <sup>*</sup>	170.0763	19.5627	0.1278	1.1259	10.759	-1.17	$4.35 \pm 0.22$	1.63
J155437.26+525526.4 <sup>*</sup>	238.6553	52.9240	0.0664	-0.5625	10.502	-1.27	$5.97 \pm 0.11$	2.30
J155539.95+212005.7 <sup>*</sup>	238.9165	21.3349	0.0709	-0.7768	10.642	-0.99	$3.26 \pm 0.12$	2.59
J132902.05+234108.4 <sup>*</sup>	202.2585	23.6857	0.0717	-0.4885	10.565	-0.94	$1.97 \pm 0.05$	2.14
J130532.91+395337.9 <sup>*</sup>	196.3871	39.8939	0.0725	-1.2688	10.653	-1.59	$3.83 \pm 0.12$	2.41
J112446.21+045525.4 <sup>*</sup>	171.1926	4.9237	0.0740	0.9605	10.729	-0.83	$2.08 \pm 0.03$	1.82
J094303.26+595809.3 <sup>*</sup>	145.7636	59.9693	0.0749	-1.2882	10.356	-1.64	$4.62 \pm 0.28$	2.43
J081403.78+261144.3 <sup>*</sup>	123.5158	26.1956	0.0757	0.5499	10.917	-0.86	$2.67 \pm 0.07$	2.22
J150844.22+260249.1 <sup>*</sup>	227.1843	26.0470	0.0826	0.3946	10.404	-1.02	$0.76 \pm 0.03$	1.86
J140648.43+062834.8 <sup>*</sup>	211.7018	6.4763	0.0850	1.1048	10.770	-1.04	$1.32 \pm 0.03$	1.87
J141235.89+411458.5 <sup>*</sup>	213.1496	41.2496	0.1025	0.0925	11.012	-1.83	$2.98 \pm 0.12$	2.48
J103753.68+391249.6 <sup>*</sup>	159.4737	39.2138	0.1068	0.5869	10.446	-0.98	$1.10 \pm 0.06$	1.78
J090924.55+192004.8 <sup>*</sup>	137.3523	19.3347	0.1072	-0.2895	10.532	-0.82	$1.78 \pm 0.10$	2.26
J075709.69+190842.8	119.2904	19.1452	0.1050	0.6167	10.767	-1.37	$3.09 \pm 0.12$	2.06
J100120.37+182926.6	150.3349	18.4907	0.1060	0.0215	10.498	-1.56	$1.45 \pm 0.06$	2.15
J101708.94+122412.0	154.2873	12.4034	0.1076	0.0808	10.567	-1.58	$6.89 \pm 0.33$	1.83

Table 1 *continued*

Table 1 (continued)

SDSS Name	R.A.	Dec	$z$	SFR	$\log M_*/M_\odot$	$\log M_{\text{dust}}$	Sérsic Index	$^{0.0}u - r$
J074547.87+265537.9	116.4495	26.9272	0.1148	0.9047	10.312	-0.78	$7.98 \pm 0.11$	1.53
J144024.32+175852.7	220.1013	17.9813	0.1157	-0.1135	10.502	-1.73	$5.68 \pm 0.39$	2.17
J151257.19+280937.5	228.2383	28.1604	0.1155	-0.8570	10.941	-1.10	$5.40 \pm 0.27$	2.52
J100809.02+154951.3	152.0376	15.8309	0.1176	0.3173	10.982	-1.10	$1.74 \pm 0.06$	2.02
J084752.78+514236.2	131.9699	51.7101	0.1200	0.8325	10.756	-1.11	$1.34 \pm 0.10$	1.75
J151117.94+221428.2	227.8248	22.2412	0.1205	-0.8159	11.116	-0.98	$4.29 \pm 0.30$	2.42
J012100.67+140517.3	20.2528	14.0881	0.1294	0.8598	10.930	-0.90	$3.23 \pm 0.18$	1.85
J000046.46+143813.0	0.1936	14.6370	0.1366	0.5935	11.053	-1.07	$3.38 \pm 0.18$	2.45
J081451.87+533732.5	123.7161	53.6257	0.1390	0.8186	10.857	-1.18	$1.72 \pm 0.10$	1.94
J104138.79+341253.5	160.4117	34.2149	0.1403	0.7567	10.902	-1.51	$5.12 \pm 0.28$	1.93
J100955.70+220949.3	152.4821	22.1637	0.1415	-0.5718	11.131	-1.19	$4.67 \pm 0.19$	2.33
J115326.76+403719.1	178.3615	40.6220	0.1451	0.8811	10.406	-1.13	$0.97 \pm 0.04$	1.54
J232452.26+154251.0	351.2178	15.7142	0.1511	0.6084	10.973	-1.58	$4.85 \pm 0.38$	1.85
J105344.12+552405.7	163.4339	55.4016	0.1517	1.1808	10.711	-1.07	$1.03 \pm 0.05$	1.62
J085959.47+092225.7	134.9978	9.3738	0.1519	1.1258	10.773	-0.74	$2.80 \pm 0.10$	1.76
J111431.83+405613.8	168.6327	40.9372	0.1525	-0.7727	11.104	-1.06	$4.68 \pm 0.43$	2.51
J100256.90+442457.8	150.7371	44.4161	0.1545	-0.5432	11.393	-0.31	$3.12 \pm 0.11$	2.72
J084157.98+052605.8	130.4916	5.4349	0.1563	0.3459	11.221	-1.04	$4.45 \pm 0.24$	2.12
J131022.77+251809.3	197.5949	25.3026	0.1604	1.1384	10.806	-1.20	$4.02 \pm 0.35$	2.16
J135241.36+000925.8	208.1724	0.1572	0.1660	0.9115	11.165	-1.12	$2.07 \pm 0.09$	2.08
J085434.65+111334.7	133.6444	11.2263	0.1672	0.8626	11.596	-0.87	$7.93 \pm 0.07$	1.97
J134105.98 -004902.5	205.2749	-0.8174	0.1754	1.0146	11.074	-1.11	$6.15 \pm 0.33$	1.58
J120145.97+352522.5	180.4416	35.4229	0.1903	0.5322	11.192	-0.68	$5.32 \pm 0.30$	2.12
J112238.84+143348.4	170.6619	14.5634	0.1942	0.9404	11.252	-1.06	$7.96 \pm 0.12$	1.76
J104609.61+165511.4	161.5401	16.9199	0.2069	0.8473	11.346	-0.81	$8.00 \pm 0.13$	1.57
J102959.95+482937.9	157.4998	48.4939	0.2324	1.5759	10.655	-0.75	$3.90 \pm 0.39$	0.85
J154029.29+005437.2	235.1221	0.9104	0.0117	-2.4216	8.322	-3.71	$1.09 \pm 0.02$	1.09
J154843.06+220812.6	237.1794	22.1368	0.0313	-0.6606	9.945	-1.42	$3.80 \pm 0.11$	2.30
J120057.93+064823.1	180.2414	6.8064	0.0360	-0.2476	11.058	-0.70	$3.38 \pm 0.02$	2.15
J142808.89 -023124.8	217.0371	-2.5236	0.0521	-0.7258	9.923	-2.22	$7.89 \pm 0.38$	2.04
J215648.45+004110.6	329.2019	0.6863	0.0539	-0.3556	10.549	-1.80	$5.83 \pm 0.20$	2.28
J004500.47 -004723.1	11.2520	-0.7897	0.0568	-0.0044	9.426	-2.20	$1.19 \pm 0.08$	1.25
J150440.39+010735.0	226.1683	1.1264	0.1283	0.6755	11.187	-0.64	$3.79 \pm 0.15$	2.14
J095754.76+020711.2	149.4782	2.1198	0.1253	0.5030	10.736	-1.42	$3.62 \pm 0.23$	2.27
J134123.20+151650.4	205.3467	15.2807	0.1255	1.0196	10.906	-1.03	$1.99 \pm 0.07$	1.89
J120942.22+320258.8	182.4259	32.0497	0.0590	0.2593	10.784	-1.36	$4.44 \pm 0.05$	2.02
J140950.27+105740.2	212.4595	10.9612	0.0597	0.3989	11.246	-0.83	$1.82 \pm 0.01$	2.32
J114922.02+544151.4	177.3418	54.6976	0.0619	0.4912	10.566	-1.72	$1.17 \pm 0.02$	1.83
J084232.87+235719.6	130.6370	23.9555	0.0635	0.4795	10.464	-2.08	$4.99 \pm 0.08$	1.69
J105145.47+210132.1	162.9395	21.0256	0.0659	-0.6158	10.304	-2.02	$4.54 \pm 0.25$	2.14
J144829.01+113732.1	222.1209	11.6256	0.0666	0.3213	10.711	-1.36	$2.28 \pm 0.04$	2.07

Table 1 continued

Table 1 (continued)

SDSS Name	R.A.	Dec	$z$	SFR	$\log M_*/M_\odot$	$\log M_{\text{dust}}$	Sérsic Index	$^{0.0}u - r$
J142420.78+624916.5	216.0866	62.8213	0.1091	0.4550	10.960	-1.56	$3.58 \pm 0.13$	2.24
J081121.40+405451.8	122.8392	40.9144	0.0670	0.8102	10.217	-1.17	$5.98 \pm 0.20$	1.90
J153310.02+272920.2	233.2918	27.4890	0.0719	-0.4336	10.972	-1.11	$4.96 \pm 0.05$	2.26
J161258.17+141617.5	243.2424	14.2715	0.0720	-0.0619	10.510	-1.39	$6.26 \pm 0.28$	1.95
J020552.15+000411.7	31.4673	0.0699	0.0765	0.8150	10.345	-0.94	$1.42 \pm 0.06$	1.70
J143016.05+230344.4	217.5669	23.0623	0.0810	-0.2164	11.228	-1.33	$3.88 \pm 0.06$	2.34
J121907.89+051645.7	184.7829	5.2794	0.0825	0.0719	10.226	-1.31	$2.19 \pm 0.11$	2.14
J152438.13+531458.7	231.1589	53.2496	0.0851	0.1311	10.011	-2.02	$1.36 \pm 0.07$	1.71
J214142.90-085702.3	325.4288	-8.9507	0.0873	-0.3762	10.499	-1.56	$2.65 \pm 0.15$	2.23
J085835.90+412113.8	134.6496	41.3539	0.0870	-1.0266	10.498	-1.06	$3.81 \pm 0.26$	2.44
J093135.46+662652.2	142.8978	66.4478	0.0873	-1.0901	10.784	-1.90	$6.06 \pm 0.28$	2.23
J124255.36+253727.9	190.7307	25.6244	0.0879	-1.3684	10.426	-1.57	$4.51 \pm 0.25$	2.51
J134032.49+184218.6	205.1354	18.7052	0.0902	-0.5332	10.609	-1.77	$5.79 \pm 0.24$	2.14
J132848.45+275227.8	202.2019	27.8744	0.0911	0.1618	10.828	-1.35	$5.86 \pm 0.21$	2.00
J083721.86+414342.0	129.3411	41.7283	0.0981	0.6995	11.010	-1.10	$3.51 \pm 0.12$	2.20
J091531.04+481407.7	138.8794	48.2355	0.1005	-0.7665	10.874	-1.54	$6.61 \pm 0.12$	2.42

\*Have multi-epoch spectroscopy from Wang et al. (2022).

<sup>a</sup>Tentative classification from Wang et al. (2022) as TDE.

<sup>b</sup>Tentative classification from Wang et al. (2022) as AGN flare.

<sup>c</sup>Tentative classification from Wang et al. (2022) as turn-on CL AGN.

## REFERENCES

- Auchettl, K., Ramirez-Ruiz, E., & Guillochon, J. 2018, ApJ, 852, 37. doi:10.3847/1538-4357/aa9b7c
- Barrows, R. S., Comerford, J. M., Stern, D., et al. 2021, ApJ, 922, 179. doi:10.3847/1538-4357/ac1352
- Bongiorno, A., Merloni, A., Brusa, M., et al. 2012, MNRAS, 427, 3103. doi:10.1111/j.1365-2966.2012.22089.x
- Brinchmann, J., Charlot, S., White, S. D. M., et al. 2004, MNRAS, 351, 1151
- Canalizo, G. & Stockton, A. 2001, ApJ, 555, 719. doi:10.1086/321520
- Clark, P., Graur, O., Callow, J., et al. 2023, arXiv:2307.03182. doi:10.48550/arXiv.2307.03182
- Dodd, S. A., Law-Smith, J. A. P., Auchettl, K., et al. 2021, ApJL, 907, L21. doi:10.3847/2041-8213/abd852
- Dong, X., Wang, T., Wang, J., et al. 2008, MNRAS, 383, 581. doi:10.1111/j.1365-2966.2007.12560.x
- Fan, X., Strauss, M. A., Schneider, D. P., et al. 2001, AJ, 121, 54. doi:10.1086/318033
- Ferrarese, L. & Ford, H. 2005, SSRv, 116, 523. doi:10.1007/s11214-005-3947-6
- Frederick, S., Gezari, S., Graham, M. J., et al. 2019, ApJ, 883, 31
- French, K. D., Wevers, T., Law-Smith, J., et al. 2020, SSRv, 216, 32
- French, K. D., Arcavi, I., & Zabludoff, A. 2017, ApJ, 835, 176. doi:10.3847/1538-4357/835/2/176
- French, K. D., Arcavi, I., & Zabludoff, A. 2016, ApJL, 818, L21
- Gadotti, D. A. 2008, MNRAS, 384, 420. doi:10.1111/j.1365-2966.2007.12723.x
- García-Bernete, I., González-Martín, O., Ramos Almeida, C., et al. 2022, A&A, 667, A140. doi:10.1051/0004-6361/202244230
- Graham, M. J., Djorgovski, S. G., Drake, A. J., et al. 2017, MNRAS, 470, 4112
- Graur, O., French, K. D., Zahid, H. J., et al. 2018, ApJ, 853, 39. doi:10.3847/1538-4357/aaa3fd
- GRAVITY Collaboration, Dexter, J., Shangguan, J., et al. 2020, A&A, 635, A92. doi:10.1051/0004-6361/201936767

**Table 2.** CL AGN host galaxy matching summary. Sérsic index errors are the median of individual Sérsic errors.

Category	Fraction	Percent	Median Sérsic Index
All MIRONG	18/103	17.5	$3.96 \pm 0.14$
AGN MIRONG	10/52	19.2	$4.32 \pm 0.14$
AGN	9,455/52,613	18.0	$3.05 \pm 0.08$
Galaxies	73,722/500,707	14.7	$4.01 \pm 0.15$

- Hammerstein, E., Gezari, S., van Velzen, S., et al. 2021, *ApJL*, 908, L20. doi:10.3847/2041-8213/abdc4
- Hammerstein, E., van Velzen, S., Gezari, S., et al. 2023, *ApJ*, 942, 9. doi:10.3847/1538-4357/aca283
- Heckman, T. M. & Best, P. N. 2014, *ARA&A*, 52, 589. doi:10.1146/annurev-astro-081913-035722
- Hickox, R. C. & Alexander, D. M. 2018, *ARA&A*, 56, 625. doi:10.1146/annurev-astro-081817-051803
- Ho, L. C. 2008, *ARA&A*, 46, 475. doi:10.1146/annurev.astro.45.051806.110546
- Jiang, N., Wang, T., Dou, L., et al. 2021, *ApJS*, 252, 32. doi:10.3847/1538-4365/abd1dc
- Kauffmann, G., Heckman, T. M., Tremonti, C., et al. 2003, *MNRAS*, 346, 1055
- Kauffmann, G., Heckman, T. M., White, S. D. M., et al. 2003, *MNRAS*, 341, 33. doi:10.1046/j.1365-8711.2003.06291.x
- Kewley, L. J., Groves, B., Kauffmann, G., et al. 2006, *MNRAS*, 372, 961. doi:10.1111/j.1365-2966.2006.10859.x
- Khabibullin, I. & Sazonov, S. 2014, *MNRAS*, 444, 1041
- Kormendy, J. & Ho, L. C. 2013, *ARA&A*, 51, 511
- Landi, R., Masetti, N., Morelli, L., et al. 2007, *ApJ*, 669, 109
- Law-Smith, J., Ramirez-Ruiz, E., Ellison, S. L., et al. 2017, *ApJ*, 850, 22
- Leloudas, G., Dai, L., Arcavi, I., et al. 2019, *ApJ*, 887, 218. doi:10.3847/1538-4357/ab5792
- Lu, K.-X., Zhao, Y., Bai, J.-M., et al. 2019, *MNRAS*, 483, 1722. doi:10.1093/mnras/sty3229
- Ma, Y.-S., Li, S.-J., Gu, C.-S., et al. 2023, *MNRAS*, 522, 5680. doi:10.1093/mnras/stad1377
- Marchesi, S., Lanzuisi, G., Civano, F., et al. 2016, *ApJ*, 830, 100. doi:10.3847/0004-637X/830/2/100
- Martin, D. C., Wyder, T. K., Schiminovich, D., et al. 2007, *ApJS*, 173, 342. doi:10.1086/516639
- Mathis, J. S., Ruml, W., & Nordsieck, K. H. 1977, *ApJ*, 217, 425. doi:10.1086/155591
- Mendel, J. T., Simard, L., Palmer, M., et al. 2014, *ApJS*, 210, 3
- Merloni, A., Bongiorno, A., Brusa, M., et al. 2014, *MNRAS*, 437, 3550. doi:10.1093/mnras/stt2149
- Milosavljević, M., Merritt, D., & Ho, L. C. 2006, *ApJ*, 652, 120. doi:10.1086/508134
- Mullaney, J. R., Pannella, M., Daddi, E., et al. 2012, *MNRAS*, 419, 95. doi:10.1111/j.1365-2966.2011.19675.x
- Peng, Y.-. jie ., Lilly, S. J., Kovač, K., et al. 2010, *ApJ*, 721, 193
- Ramos Almeida, C. & Ricci, C. 2017, *Nature Astronomy*, 1, 679. doi:10.1038/s41550-017-0232-z
- Ramos Almeida, C., Levenson, N. A., Rodríguez Espinosa, J. M., et al. 2009, *ApJ*, 702, 1127. doi:10.1088/0004-637X/702/2/1127
- Raouf, M., Smith, R., Khosroshahi, H. G., et al. 2021, *ApJ*, 908, 123. doi:10.3847/1538-4357/abd47d
- Ricci, C., Trakhtenbrot, B., Koss, M. J., et al. 2017, *Nature*, 549, 488. doi:10.1038/nature23906
- Rosario, D. J., Santini, P., Lutz, D., et al. 2012, *A&A*, 545, A45. doi:10.1051/0004-6361/201219258
- Roth, N., van Velzen, S., Cenko, S. B., et al. 2021, *ApJ*, 910, 93. doi:10.3847/1538-4357/abdf50
- Sazonov, S., Gilfanov, M., Medvedev, P., et al. 2021, *MNRAS*, 508, 3820. doi:10.1093/mnras/stab2843
- Simard, L., Mendel, J. T., Patton, D. R., et al. 2011, *ApJS*, 196, 11
- Somalwar, J. J., Ravi, V., Dong, D., et al. 2022, *ApJ*, 929, 184. doi:10.3847/1538-4357/ac5e29
- Strotjohann, N. L., Saxton, R. D., Starling, R. L. C., et al. 2016, *A&A*, 592, A74
- Tadhunter, C., Spence, R., Rose, M., et al. 2017, *Nature Astronomy*, 1, 0061. doi:10.1038/s41550-017-0061
- Toba, Y., Ueda, Y., Gandhi, P., et al. 2021, *ApJ*, 912, 91. doi:10.3847/1538-4357/abe94a
- Tremonti, C. A., Heckman, T. M., Kauffmann, G., et al. 2004, *ApJ*, 613, 898. doi:10.1086/423264
- Trump, J. R., Sun, M., Zeimann, G. R., et al. 2015, *ApJ*, 811, 26. doi:10.1088/0004-637X/811/1/26
- van Velzen, S. 2018, *ApJ*, 852, 72. doi:10.3847/1538-4357/aa998e



Wang, Y., Jiang, N., Wang, T., et al. 2022, ApJS, 258, 21.  
doi:10.3847/1538-4365/ac33a6

Yan, L., Wang, T., Jiang, N., et al. 2019, ApJ, 874, 44.  
doi:10.3847/1538-4357/ab074b

Yang, Q., Wu, X.-B., Fan, X., et al. 2018, ApJ, 862, 109

Yao, Y., Ravi, V., Gezari, S., et al. 2023, ApJL, 955, L6.  
doi:10.3847/2041-8213/acf216